

Received 27 June 2024, accepted 2 August 2024, date of publication 8 August 2024, date of current version 19 August 2024.

Digital Object Identifier 10.1109/ACCESS.2024.3440635

APPLIED RESEARCH

Room Reconstruction Based on Bi-Static mmWave RADAR Using the Antenna Pattern Information

LARA WIMMER¹, MARKUS PETRI¹, AND ECKHARD GRASS^{1,2}

¹IHP-Leibniz-Institut für innovative Mikroelektronik, 15236 Frankfurt (Oder), Germany

²Department of Computer Science, Humboldt University of Berlin, 12489 Berlin, Germany

Corresponding author: Markus Petri (petri@ihp-microelectronics.com)

The authors acknowledge the financial support of this work by the German Federal Ministry for Education and Research (BMBF) within the project “Open6GHub” under grant reference number 16KISK009.

ABSTRACT Joint communication and sensing (JCAS) is one of the key topics of the upcoming 6G mobile communication standard. We propose a novel three-step method to extract the position of reflectors from channel impulse responses (CIRs) obtained by multiple bi-static RADAR measurements. The method consists of the extraction of angle-of-departure (AoD) and angle-of-arrival (AoA), the computation of potential reflecting points and the classification of the propagation paths. For the extraction of AoD and AoA, we propose a novel algorithm with low computational effort. It has a better resolution than the step size of the underlying beam search process by utilizing the antenna beam pattern together with the evaluation of the CIR. The algorithm is compared to a straightforward approach in a raytracing simulation. The evaluation shows that the proposed novel algorithm outperforms the state-of-the-art approach. Furthermore, we discuss the limitations of the proposed room reconstruction method and the potential impacts of physical effects not covered in the simulation.

INDEX TERMS 6G, bi-static RADAR, joint communication and sensing (JCAS), room reconstruction.

I. INTRODUCTION

Joint Communication and Sensing (JCAS / JCS), sometimes also called Integrated Sensing and Communication (ISAC), has gained a lot of interest in recent years. Especially, the current research on the 6th generation of mobile networks (6G) focuses on the integration of JCAS [1], [2], [3]. This will enable certain new use cases for mobile networks, like traffic management and environmental monitoring. A good overview of sensing applications is presented in [4].

One main element to enable the intended use cases of JCAS is a digital twin as a virtual representative of the physical world [5]. While this digital twin can be a comprehensive digital world including physical entities, its basic form can be a representation of the RF propagation environment, i.e., the RF channel characteristics. Such a basic digital twin can

be exploited for sensing-assisted communication, e.g., for fast beam training and predictive beamforming [6].

A fundamental task for creating a digital twin of the RF surrounding is room reconstruction, i.e. the initial localization of static objects like walls and furniture determining the general propagation characteristics. Furthermore, the current positions of moving objects have to be included and the digital twin needs to be continuously updated. The general idea of JCAS-based room reconstruction is the use of channel measurements from the communication link to extract the reflection paths and to estimate the positions of the reflectors, e.g. walls.

In this paper, we propose a new algorithm for estimating the positions of reflectors. It evaluates the channel impulse response (CIR) obtained by a bistatic RADAR measurement, deploying a mmWave communication system for this sensing function. In contrast to the current algorithms, the new algorithm avoids the noise enhancement of zero-forcing methods. Furthermore, it has a better angular resolution than

The associate editor coordinating the review of this manuscript and approving it for publication was Cheng Hu .

the step size of the underlying beam search process by utilizing the antenna beam patterns during the evaluation of the CIR. Last, it has a lower computational effort, since it does not require matrix inversions or singular-value decompositions. We also present a method to classify the identified reflective paths in terms of the number of reflections (direct, single or multiple reflections). The proposed algorithm is compared to a straight-forward and simple 'find maximum' approach. The latter one just detects the highest peak in the CIR and uses the beam angles of transmitter and receiver to define the angles of departure and arrival, respectively.

This paper is organized as follows: In Section II, we summarize the state-of-the-art in room reconstruction by wireless measurements. In Section III, we present raytracing simulation methods used to create the CIRs and the room reconstruction algorithm. Section IV deals with the simulation results, while the findings and limitations of the approach are discussed in Section V. A conclusion and an outlook are given in Section VI.

II. STATE OF THE ART

Not only the detection of moving targets with RADAR, but also the reconstruction of the local surrounding and static objects by wireless measurements has been of interest for a long time. The main technologies found in literature are RF signal transmission, laser scanning and acoustic measurements. Laser scanning has been applied in [7] to generate a complete 3D model of an indoor environment. While the accuracy of the reconstructed room is very good, this approach does need a specific laser scanning device.

Room reconstruction by RF signal transmission or acoustic measurements is mainly based on the reflection of the transmitted signals at walls and objects. The main task is to estimate the direction of arrival of the received signal, i.e. the angle of the incoming wavefront. Based on the departure and arrival angles as well as the length of the signal path, the position of the reflectors can be calculated. The *Multiple Signal Classification (MUSIC)* [8] and *Estimation of Signal Parameters via Rotational Invariance Techniques (ESPRIT)* [9] algorithms were well studied and used in a broad variance of applications to estimate the direction of signal sources with arrays of receiving sensors.

In case of phased arrays using beamforming for data transmission, *MUSIC* and *ESPRIT* can be only used for digital beamforming systems with an individual sampling of the signals for all antenna elements due to the principle of the algorithm. Nevertheless, adaptations have been proposed to use them also with analog beamforming [10], where only the summed signal of all antenna elements is available for further processing. Here, a full beam search is done to obtain the data, making use of a quasi-static environment during beam scanning.

Besides *MUSIC* and *ESPRIT*, others algorithms and methods have been proposed. [11] uses the Kirchhoff migration to detect walls of a room using an ultra-wideband

(UWB) system. It is based on a moving receiver. Due to the very high bandwidth of the UWB signal, a very high spatial resolution can be achieved. This method is transferred to mmWave beamsteering systems in [12]. It is furthermore enhanced by using the angle of departure (AoD) and angle of arrival (AoA). While the walls of the surrounding room can be much better detected, the method still needs a moving receiver to be able to detect static objects.

In [13], two methods for room reconstruction based on a static transmitter and a static receiver are presented. The first method is based on a power heat-map of the received signal strength over different TX / RX beam combinations. The authors also suggest an enhanced method, using the time delay of the signals between a direct (line-of-sight, LoS) and a reflective (non-line-of-sight, NLoS) path. While the good performance of the second method was evaluated in a real measurement, it is a pure RADAR approach with a complete environmental scanning. It does not use the information about NLoS components already included in the CIR, which could e.g. be extracted from a data frame of a wireless communication link.

Compressed sensing based approaches using simultaneous orthogonal matching pursuit (SOMP) and multidimensional representation MOMP are proposed in [14] resp. [15], using the sparsity of the channel information in an mmWave environment.

The authors of [16] use a convolutional neural network (CNN) to determine the room geometry based on acoustic measurements. The proposed method does not require the position or distance of receivers and sources. It only requires one room impulse response between a single sound source and a single receiver. A multilayer perceptron (MLP) neural network is used in [17] to estimate the room shape. In this study, the network is previously trained with radio wave propagation parameters like power delay profile, angle of departure and angle of arrival, to predict the room shape based on channel measurements. Another acoustic method for room reconstruction is shown in [18]. It also does not require a priori information about the position of sound sources and microphones. A third acoustic approach using image processing to approximate wavefronts and graph-theory is given in [19].

The presented methods for mmWave RF signal based room reconstruction are either of high computational effort, are not able to use an analog beamforming approach or require the use of a moving receiver. In contrast, our proposed room-reconstruction algorithm uses static transceivers with analog beamformers, allowing for a much more energy-efficient implementation compared to digital beamforming [20]. Furthermore, it is based on pattern matching with low computational effort in contrast to singular-value decomposition required for *MUSIC*.

For our method, classifying the reflection type of the identified path is essential. While we use an analytical approach, other methods are applicable. In [21], a deep neural network based non-line-of-sight identification method

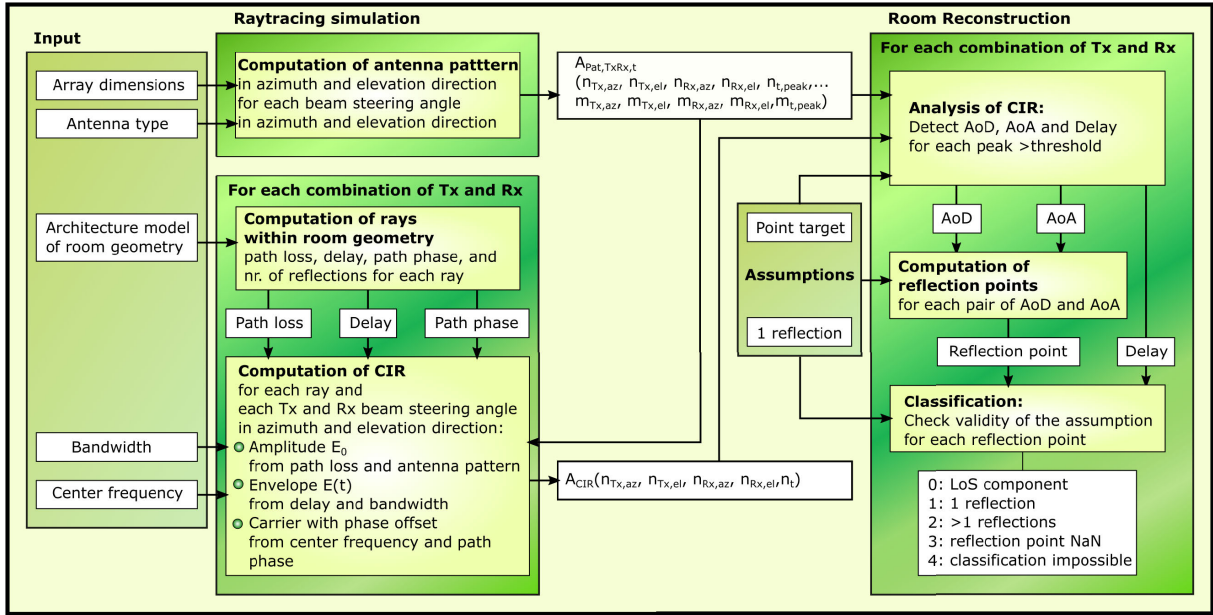


FIGURE 1. Flow chart of the raytracing simulation and the room reconstruction algorithm.

is proposed. This could be an extension for our classification algorithm as discussed in Section IV.

III. ALGORITHMS AND SIMULATION METHODS

The reconstruction of the reflection points is performed using simulated CIRs as an input in order to study the performance of our reconstruction algorithm. In this Section, the simulation for generating the CIRs is explained as well as the algorithm to reconstruct the reflection points in 3D. This algorithm includes a step to classify multipath components in a CIR into the line-of-sight contribution, rays with one reflection and rays received after more than one reflection.

Figure 1 shows a flow chart of the simulation generating the CIRs (left side) interacting with the program for room reconstruction (right side).

A. RAYTRACING SIMULATION

The CIRs are simulated using MATLAB's raytracing capabilities in a specific room geometry. For the reconstruction of the reflection points in 3D, the antenna array patterns and the temporal shape of the transmit pulse have to be known. This part of the simulation is shown in Fig. 1 on the left side with all required input files and parameters.

1) COMPUTATION OF THE CHANNEL IMPULSE RESPONSES

The CIRs are computed for the exemplary scenario of an indoor office environment that is inspired by shared common room offices. This scenario is depicted in Fig. 2. The room is designed with the architecture software Revit LT [22] (s. Fig.: 2a) and has a size of $8 \times 10 \times 4 \text{ m}^3$. 10 transmitters and 2 receivers are distributed in 1 m height along the walls of the rooms. The arrays consist of $n \times m$ patch antennas that are separated by a distance x and rotated in a way, that for a beam steering angle of 0° (no phaseshift between the antennas in

the array), the main lobe of the beam is pointing orthogonally away from the wall (s. Fig.: 2b).

The non-line-of-sight (NLoS) components of the CIR are computed using a shooting and bouncing rays method following the reflection condition, according to which the incident angle is equal to the angle of the reflected beam. All rays from all Rx and Tx combinations are shown in the office room in Fig. 2c. The raytracing algorithm is already embedded in MATLAB's *raytrace* function, which provides the path loss p_{PL} , phase α , delay t_d , AoD, and AoA in azimuth and elevation direction of the respective rays. The components of the CIR are modeled as bandwidth-limited Gaussian pulses in time with a carrier frequency f_c of 60 GHz and a bandwidth bw of 2 GHz:

$$E(t) = E_0 \cdot e^{-\frac{\pi^2 bw^2}{2 \ln 2} (t_i - \bar{t})^2} \cdot e^{i2\pi f_c t_d + \alpha}, \quad (1)$$

where $E(t)$ denotes the electric field at time t . This expression comes from the slowly varying envelope approximation (SVEA). The amplitude E_0 is given by the path loss p_{PL} and the gain in dB at Tx p_{Tx} and Rx p_{Rx} in the angles of departure and arrival for the respective beam steering directions:

$$E_0 = e^{(p_{Tx}(\phi, \theta) - p_{PL} + p_{Rx}(\phi, \theta)) / 20}. \quad (2)$$

To compute the CIR, the individual components are following the superposition principle, i.e., they are added in complex plane.

Unrealistic rays with angles of departure and arrival $\geq |90^\circ|$ leaving or approaching the antenna array on its backside are excluded. The simulated channel responses consist of reflected rays without adding artificial noise in order to study the fundamental limits of the reconstruction algorithm. Scattering and diffraction or the polarization of the transmitted signal are also not included. Figure 3 shows two exemplary CIRs with the accumulated signals of all

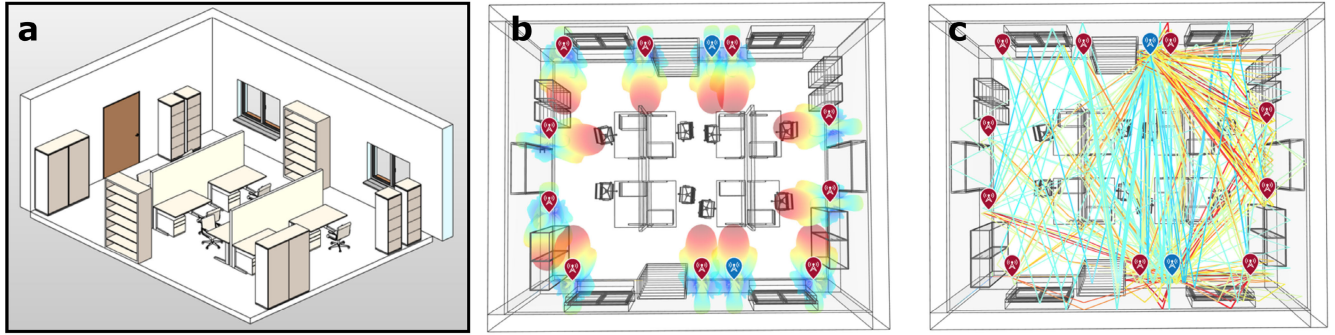


FIGURE 2. Raytracing simulation in an office room. a: Side view with front walls removed. b: Top view with Tx (red) and Rx (blue) antenna arrays, all with 0° beam steering angle. c: Direct and reflected rays between all Rx and Tx. Red: low path loss, blue: High path loss.

Tx at both receivers for a beam steering angle of 0°. It illustrates that for the given room geometry, a large number of reflection peaks appear. Some reflection peaks are partially overlapping, which is challenging for a reconstruction of the reflection points.

We compute CIRs for steering angles of ±60° in azimuth and ±20° in elevation, both with a step size of 10°. The set of CIRs employed to compute the reflection points contains the individual CIRs for all possible combinations of beam steering angles between the N transmitters and M receivers. The information can be written in an array A_{CIR} with dimensions

$$\dim(A_{CIR}) = N \times M \times n_{Tx,az} \times n_{Tx,el} \times n_{Rx,az} \times n_{Rx,el} \times n_t, \quad (3)$$

where $n_{Tx,az}$ and $n_{Tx,el}$ are the number of azimuth and elevation beam steering angles for the transmitter, $n_{Rx,az}$ and $n_{Rx,el}$ are the number of angles for the receiver and n_t is the number of sampling points on the time axis. $A_{CIR}(1,2,1,1,2,1,1:600)$ would, therefore, give the first 600 samples of the CIR between transmitter 1 and receiver 2, using the transmitter beam 1 in both, azimuth and elevation as well as the receiver beam 2 in azimuth and 1 in elevation.

This corresponds to the information obtained by an exhaustive beam search procedure between two connecting nodes. The maximum of the time axis is 100 ns, which corresponds to a transmission distance of ≈ 30 m. Considering the size of the room, the length of the time axis is sufficient to cover all rays with one reflection: The room diagonal is $\sqrt{8^2 + 10^2 + 4^2} = 13.42$ m. Thus, the maximum expected path length for the first reflection order is 26.83 m.

The number of reflections is limited to two in order to keep the computation time at bay. Only peaks coming from rays with one reflection can be accessed analytically without further information (s. Par.: III-B). In our reconstruction algorithm, peaks from rays with more than one reflection are sorted into one common class and neglected. The exact number of reflections does not matter.

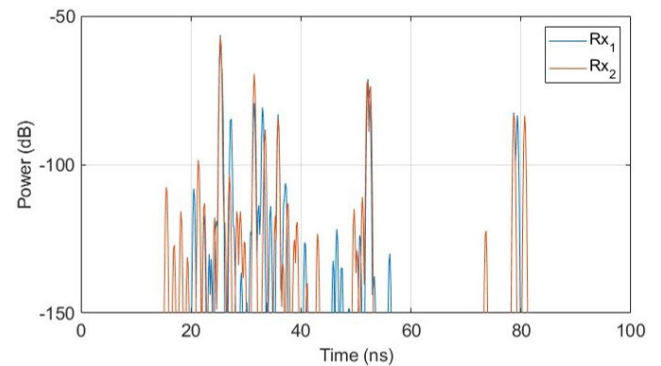


FIGURE 3. Accumulated CIRs with simultaneous transmission from all Tx, received at Rx_1 and Rx_2 . Array size: 4 antennas in horizontal direction, 2 in vertical direction.

2) EFFECT OF THE ANTENNA PATTERN

As described in the previous paragraph, each component in the CIR is affected by the patterns of the Tx and Rx antenna arrays and by the temporal shape of the transmitted pulse. Taking a combination of a receive antenna array with a 1D scanning capability and an omnidirectional transmit antenna in an empty anechoic chamber as a simple example, the received signal \vec{s}_{Rx} is the transmitted signal \vec{s}_{Tx} multiplied with the matrix $A_{Pat,1D}$:

$$\vec{s}_{Rx} = A_{Pat,1D} \vec{s}_{Tx}. \quad (4)$$

Each row in the matrix $A_{Pat,1D}$ indicates one beam steering angle and the columns are the sampling points of the respective antenna pattern. Examples of one-dimensional antenna patterns for a perpendicular beam and different array sizes are shown in Fig. 4.

The effect of the antenna pattern on the received signal can be seen as a kind of convolution of the transmit signal with the antenna pattern. This is a convolution with a variable convolution kernel since the antenna pattern is depending on the beam steering angle. \vec{s}_{Tx} is a column vector, where each line corresponds to a different azimuth angle. \vec{s}_{Tx} is one for the angle, in which the Tx is placed relative to the Rx and zero otherwise.

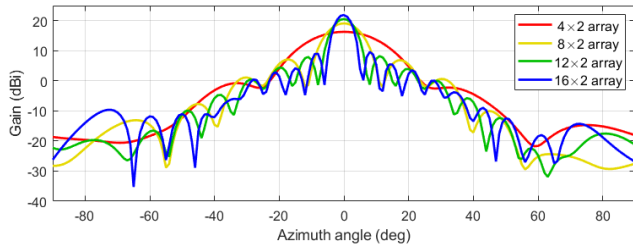


FIGURE 4. Antenna patterns in azimuth direction, 0° elevation, for different array sizes and 0° steering vector.

Multiplying the inverted Matrix A_{Pat}^{-1} with the received signal without noise would restore the original signal. Unfortunately, every real-world system comes with noise. This kind of “zero-forcing deconvolution” leads to noise enhancement and is thus in practice often of no use. A better choice are algorithms that aim for a maximum likelihood deconvolution and can handle a varying convolution kernel, e.g., the *Lucy-Richardson* algorithm [23], [24] or the *Viterbi* algorithm [25]. An example for the application of the *Lucy-Richardson* algorithm is given in [26]. Other suitable algorithms can be found in the areas of channel equalization, image processing, and acoustics [27], [28], [29], [30], [31].

However, in order to restore the original features of the ray, i.e., AoD, AoA, and delay, the antenna patterns and the temporal shape of the pulse have to be known for most of these algorithms. Only blind or semi-blind equalization techniques might be an exception but will be most likely inferior to ML methods with a prior knowledge of the antenna patterns.

For a 2D beamsteering system, the antenna patterns in azimuth and elevation for each possible pair of beam steering angles in azimuth and elevation direction can be stored in an array $A_{Pat,2D}$ according to $A_{Pat,1D}$, with dimensions

$$\dim(A_{Pat,2D}) = n_{az} \times n_{el} \times m_{az} \times m_{el}, \quad (5)$$

where n_{az} is the number of beams in azimuth, n_{el} the number of beams in elevation, and m_{az} and m_{el} are the numbers of sampling points for the appropriate azimuth elevation antenna pattern, respectively. Thus, $A_{Pat,2D}(1,2,:,:)$ represents the two-dimensional antenna pattern (sampled in azimuth and elevation) for the beam index 1 in azimuth and index 2 in elevation. All possible combinations of Tx and Rx angles result in a structure with twice as many dimensions as $A_{Pat,2D}$.

As mentioned, the CIRs are not only affected by the antenna patterns, but also by the temporal shape of the transmitted pulse. To include the temporal shape with a higher resolution than the temporal resolution of the CIR, a matrix representing the pulse samples for different sub-sample offsets according to Fig. 5 is generated. This matrix is combined with the structure representing all possible combinations of TX and RX beam patterns, finally forming the structure $A_{Pat,TxRx,t}$.

The structure $A_{Pat,TxRx,t}$ contains all additional information used for the evaluation of the CIRs given by A_{CIR} . Its

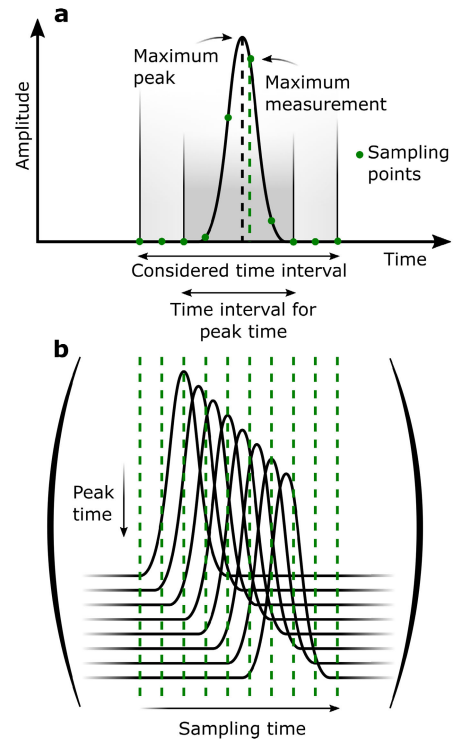


FIGURE 5. Generation of a matrix representing the pulse timing with different sub-sample timing offsets **a:** The pulse amplitude as a function of time as a black line, the pulse measured with a limited sampling rate indicated by the green dots. **b:** Matrix with the timing information. Each line contains the measurements with the given sampling rate (green dashed line). Each line stands for a different peak time (path delay) and the target time resolution is determined by difference between the peak times in the different lines.

size is given by:

$$\begin{aligned} \dim(A_{Pat,TxRx,t}) &= n_{Tx,az} \times n_{Tx,el} \times n_{Rx,az} \times n_{Rx,el} \\ &\times m_{Tx,el} \times m_{Tx,az} \times m_{Rx,el} \times m_{Rx,az} \\ &\times n_{t,peak} \times m_{t,peak}. \end{aligned} \quad (6)$$

$n_{t,peak}$ is the number of sampling points in the time span t_{peak} , which a single multipath component of the CIR is affecting. $m_{t,peak}$ is the number of different arrival times within the sampling time covered by $n_{t,peak}$. $m_{t,peak}$ determines the target time resolution of the reconstruction algorithm: For each arrival time t_j ($j = 1, 2, \dots, n_{t,peak}$) within t_{peak} , the power measured at the sampling points $k = 1, 2, \dots, n_{t,peak}$ is computed and multiplied by the antenna pattern. In this way, a five-dimensional representation (azimuth and elevation of Tx and Rx plus time) of a possible component of the CIR is constructed.

3) SYSTEMATIC ANGULAR ANALYSIS

The angles of the reflected rays depend on the room geometry and are determined by the reflection condition. In order to evaluate the performance of the angle detection systematically, we created an artificial data set that is independent of the room geometry. For that, we skipped the temporal component in (3) to create the structure B_{CIR} for

all combinations of Tx and Rx angles with azimuth angles in between $\pm 60^\circ$ with a step size of 5° and elevation angles between $\pm 30^\circ$, also with a step size of 5° . The dimensionality of the structure B_{CIR} is equal to the CIRs in the room A_{CIR} (cf. (3)) except for the last (temporal) dimension:

$$\dim(B_{CIR}) = n_{Tx,az} \times n_{Tx,el} \times n_{Rx,az} \times n_{Rx,el}. \quad (7)$$

The size of the structure containing the antenna pattern $B_{Pat,RxTx}$ is reduced by the two temporal dimensions compared to the structure $A_{Pat,RxTx,t}$ described in (6):

$$\begin{aligned} \dim(B_{Pat,RxTx}) &= n_{Tx,az} \times n_{Tx,el} \times n_{Rx,az} \times n_{Rx,el} \\ &\quad \times m_{Tx,az} \times m_{Tx,el} \times m_{Rx,az} \times m_{Rx,el}. \end{aligned} \quad (8)$$

B. ROOM RECONSTRUCTION ALGORITHM

Figure 1 shows our algorithm to compute the reflection points in 3D on the right side. The flow chart also includes our assumptions and what kind of structures are taken from the raytracing simulation. The algorithm needs the antenna patterns in 2D for all measured beam steering angles $A_{Pat,RxTx,t}$ (cf. (6)) together with the data set from the beam search process A_{CIR} (cf. (3)) as an input to perform the following three steps consecutively for all possible combinations of Tx and Rx:

- **Analysis of the CIRs:** Extraction of the AoD, AoA, and the delay of all components of the CIR.
- **Computation of the reflection points** from the angles of departure and arrival.
- **Classification** of the rays into five categories:
 - 1) Line-of-Sight components,
 - 2) rays with one reflection,
 - 3) rays with more than one reflections,
 - 4) rays with “NaN” (“Not a number”) elements in the reflection point coordinates, and
 - 5) rays that cannot be categorized.

These steps are described in detail in the next paragraphs.

a: ANALYSIS OF THE CIR

In this part of the algorithm, the AoD, the AoA, and the path delay of the peaks in the CIR are extracted for all possible combinations of Tx and Rx. First, the highest peak is evaluated, the angular and temporal information stored and then, the peak is deleted and the algorithm proceeds with the next highest peak. This is done, until the peak height falls below a threshold (here: 25 dB) compared to the highest peak or the maximum number of peaks (here: 15) is reached. The first condition emulates the limited dynamic range of hardware available for experiments.

The AoD and AoA are detected in the local coordinates of the respective antenna arrays. This expression is required for a later evaluation of the detection algorithm. However, for the computation of the possible reflection points, the angles need to be transferred to global coordinates.

For each detected peak, the simulated ray which is closest in delay is selected to compare our results with the original angles and delays from the simulation.

We compare two different approaches to extract the angular and temporal information from the peaks within the CIR. The first and simple method, referred to as ‘*find maximum*’ approach, is to search for the maximum within the five-dimensional CIR structure A_{CIR} (cf. (3)) of the beam search process. In this way, the results are provided with the resolution of the scanning process (here: 10° in angle and 167 ps in time), which leads to 2.5° angular deviation and 42 ps time difference in average. This method also relies on a relatively decent beam pattern, where the maximum of the pattern is found in the direction of the beam steering angle. Considering the quality of some measured antenna patterns and the noise within measurement data, this condition might not be always fulfilled.

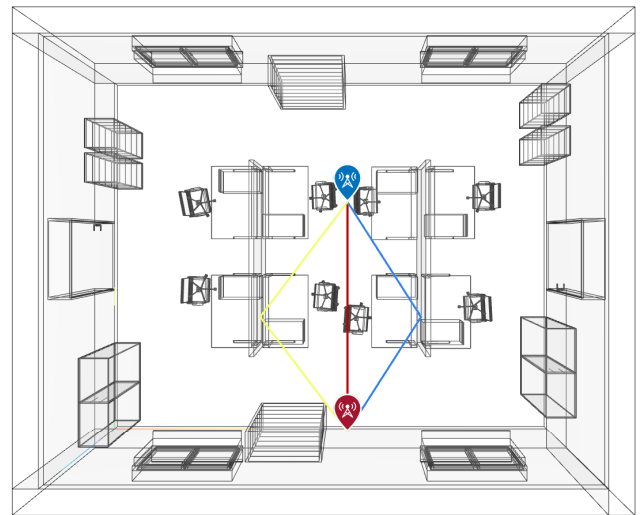


FIGURE 6. Simple beam scan scenario with one TX, one RX and two reflections.

The ‘*find maximum*’ approach and its main issue can be visualized using a 1D beam scanning approach, i.e. just a beam scan in azimuth, and a simple scenario with one direct path and two reflections as shown in Fig. 6. In this example, the angles of departure and arrival of the reflected rays are roughly $\pm 35^\circ$. We use a 4 patch antenna array with a relatively wide beam and the beam scan settings described above. For the sake of simplicity, we omit the temporal component and accumulate the received power. The accumulated received power for every beam combination is shown in Fig. 7. While the line of sight path would be correctly identified with the ‘*find maximum*’ approach, the next peaks will be identified at the AoD/AoA combinations of $0^\circ/\pm 20^\circ$ and $\pm 20^\circ/0^\circ$. The power of the expected peaks at beam combinations $\pm 40^\circ/\pm 40^\circ$ is much lower. This results from the antenna beam pattern with a wide main lobe and the coarse beam scanning granularity.

In our second approach, the ‘*compare patterns*’ approach, we make use of additional information to improve the

detection of the reflected peaks. First of all, we include the antenna patterns, sampled with a higher resolution compared to the beam scan resolution. Second, we include the Gaussian temporal shape of the CIR peaks, by using an increased temporal resolution. This finally gives the ten-dimensional array $A_{Pat, TxRx, t}$ of (6).

The five-dimensional CIR structure A_{CIR} resulting from a two-dimensional beam scanning is compared with the ten-dimensional array $A_{Pat, TxRx, t}$, finding the best pattern fit. This comparison is realized by a correlation of A_{CIR} with the array $A_{Pat, TxRx, t}$. Since the size of a ten-dimensional array easily exceeds the capabilities of processing hardware, we limited the structure to a region of interest in the surrounding of peaks identified with the 'find maximum' approach. Thus, the algorithm consists of the following steps:

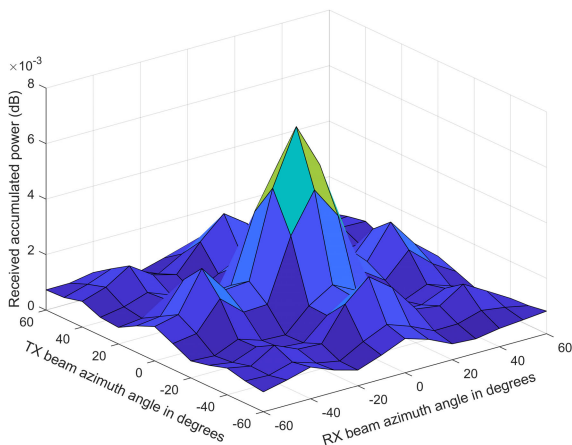


FIGURE 7. Received power for one-dimensional beam scan at TX and RX.

- 1) Find the maximum peak in the five-dimensional CIR array A_{CIR}
- 2) Extract a cutout region of interest
- 3) Generate a ten-dimensional comparison matrix of the antenna patterns and temporal pulse shapes in the cutout region
- 4) Correlate the cutout region of interest with the comparison structure.
- 5) Identify the correlation peak and extract AoD, AoA and ToF
- 6) Remove the maximum peak from the five-dimensional CIR array and repeat the algorithm until a pre-defined peak limit is reached.

Further details of the processing steps are presented in subsection C - Computational Complexity Analysis.

To explain the approach more intuitively, we use again the one-dimensional example from Fig. 7. Including the information about the antenna patterns in a comparison structure, we do not just search for the maximum peak. Instead, we find the point where the multiplied gains of the TX and RX antenna fits best to the received power. Fig. 8 shows a graphical comparison of both approaches. The black ball shows the real point target, and the grey one the target reconstruction using the 'find maximum' approach. The latter

one maps all targets within the current beam (indicated by the dark grey shaded array) to the same reconstructed angle, i.e. the current beam angle. The width of this sector is determined by the beam scanning step size. In contrast, only angles within the red shaded range are mapped onto the same reconstructed angle when using the 'compare patterns' approach. The width of this sector is determined by the accuracy of the initial pattern measurement.

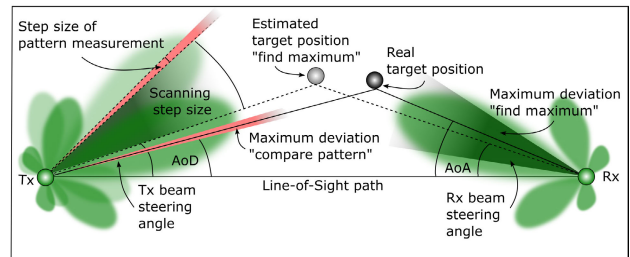


FIGURE 8. Reconstruction of a point target using the "find maximum" and the "compare pattern" method for comparison.

During the comparison of the CIR structure with $A_{Pat, TxRx, t}$, all dimensions are treated simultaneously, since a separate treatment would consider less information and hence result in worse results. Handling all dimensions separately could mean adding over the respective other dimensions, thus losing accuracy especially for noisy measurements and the ability to detect multiple peaks at the same time unambiguously. This is the main difference to an interpolation, which would also result in a higher resolution in time and space, but might lead to results deviating from the true shapes of the structures.

The 'compare patterns' method avoids the noise enhancement of zero-forcing methods and allows for "super-resolution" detection of the angles and the delay, i.e., a resolution, which is higher than the step size of the beam search process and higher than the main lobe of the antenna array pattern. This capability is due to the assumption of point targets and it requires linearly independent antenna pattern for each possible angle. Without prior knowledge of the target's characteristics, the resolution is limited by the step size of the angular scan.

This step of the algorithm is the only part of the simulation that cannot be transferred to arbitrary measurements because it is based on the assumption of point targets, which is certainly true for our simulated CIRs and maybe also for small targets in a sufficiently large distance from the Tx and Rx, but not for objects that extend over a range of angles, either AoD, AoA, or both.

Table 1 summarizes the advantages and disadvantages of both presented methods.

b: COMPUTATION OF THE REFLECTION POINTS

The reflection points within the room are computed from the angular information within the CIRs. The position and the orientation of the Tx and Rx in the room are presumed to be known. In order to compute the reflection points from the

TABLE 1. Comparison of advantages (green) and disadvantages (red) for the ‘find maximum’ and the ‘compare patterns’ approach.

‘find maximum’	‘compare patterns’
low complexity	medium complexity
Resolution limited by step size of beam scan	Resolution limited by resolution of antenna pattern
High noise sensitivity: Angle determined by maximum	Low noise sensitivity: Angle determined from range of angles
Worse results for wide beams due to decrease noise resilience	Better results for wide beams due to increased noise resilience
Complicated antenna pattern without clear maximum cannot be used	Algorithm can deal with complicated antenna pattern without clear maximum

AoD and AoA, rays with only one reflection are assumed. This assumption is reassessed afterwards in the classification step. However, in order to reconstruct reflection points analytically, first order reflections are assumed because reflection paths with more than one reflection cannot be assessed analytically in an unambiguous way. For two or more reflections, different paths and reflection points are possible with one and the same set of AoD, AoA, and delay. This can be illustrated by creating an arbitrary path with two reflection points and mirroring it at an axis between Tx and Rx as depicted in Fig. 9. This figure shows just two exemplary solutions (path a and path b) with the same set of AoD, AoA, and delay.

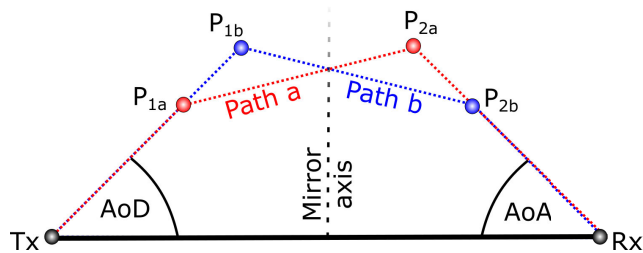


FIGURE 9. Two paths (a and b) with two reflection points and the same set of AoD, AoA and path length. P_{1a} and P_{2a} are the reflection points for path a and P_{1b} and P_{2b} for path b.

The rays from transmitter and receiver can be described as lines in a 3D vector space. The support vector of the line is given by the position vectors (\vec{S}_{Tx} and \vec{S}_{Rx}) of the respective Tx and Rx:

$$\vec{S}_{Tx} = \begin{pmatrix} Tx(1) \\ Tx(2) \\ Tx(3) \end{pmatrix} \quad (9)$$

$$\vec{S}_{Rx} = \begin{pmatrix} Rx(1) \\ Rx(2) \\ Rx(3) \end{pmatrix}. \quad (10)$$

The direction vectors are determined by the AoD and AoA in global coordinates:

$$\vec{D}_{Tx} = \begin{pmatrix} \cos(\phi_{AoD}) \cdot \cos(\theta_{AoD}) \\ \sin(\phi_{AoD}) \cdot \cos(\theta_{AoD}) \\ \sin(\theta_{AoD}) \end{pmatrix} \quad (11)$$

$$\vec{D}_{Rx} = \begin{pmatrix} \cos(\phi_{AoA}) \cdot \cos(\theta_{AoA}) \\ \sin(\phi_{AoA}) \cdot \cos(\theta_{AoA}) \\ \sin(\theta_{AoA}) \end{pmatrix}. \quad (12)$$

$z_{Tx/Rx}$ is the scalar variable that goes through all points of the line. Without any error, these two lines

$\vec{x}_{Tx/Rx} = \vec{S}_{Tx/Rx} + z_{Tx/Rx} \cdot \vec{D}_{Tx/Rx}$ would intersect and the intersection is at the reflection point. Unfortunately, there are measurement errors, noise, and the detection of the angles comes with deviations due to the step size of the angles and with errors. If the Tx and Rx line do not intersect, we assume that the most likely reflection point can be found in the following way, as illustrated in Fig. 10: We search for the center of the shortest connecting line between the Tx and the Rx line. This line has a direction vector that has to be orthogonal to the Tx and Rx direction vectors:

$$c\vec{D}_{con} = \vec{D}_{Tx} \times \vec{D}_{Rx}. \quad (13)$$

To compute the two intersection points of the connecting line with the Tx and the Rx line, we create a plane with the Tx support vector \vec{S}_{Tx} as support vector and the Tx directional vector \vec{D}_{Tx} and the directional vector of the connecting line \vec{D}_{con} as directional vectors of the plane x_{plane} :

$$c\vec{x}_{plane} = \vec{S}_{Tx} + z_1 \cdot \vec{D}_{Tx} + z_2 \cdot \vec{D}_{con}, \quad (14)$$

z_1 and z_2 are the running variables of the plane. The intersection of this plane with the Rx line is the first intersection point, where the Rx connecting line intersects the Rx line. The equation system to be solved to get the first (Rx) intersection point is:

$$\vec{x}_{plane} = \vec{x}_{Rx}, \quad (15)$$

$$\vec{S}_{Tx} + z_1 \cdot \vec{D}_{Tx} + z_2 \cdot \vec{D}_{con} = \vec{S}_{Rx} + z_{Rx} \cdot \vec{D}_{Rx}. \quad (16)$$

The first (Rx) intersection point $\vec{S}_{Rx,con}$ can serve as a support vector for the connecting line $\vec{x}_{con} = \vec{S}_{Rx,con} + z_{con} \cdot \vec{D}_{con}$. Now, the second (Tx) intersection point $\vec{S}_{Tx,con}$ can be computed as the intersection between the Tx line and the connecting line:

$$\vec{x}_{Tx} = \vec{x}_{con}, \quad (17)$$

$$\vec{S}_{Tx} + z_{Tx} \cdot \vec{D}_{Tx} = \vec{S}_{Rx,con} + z_{con} \cdot \vec{D}_{con}. \quad (18)$$

In the middle of the two points $\vec{S}_{Rx,con}$ and $\vec{S}_{Tx,con}$ is our most likely reflection point \vec{S}_R :

$$\vec{S}_R = \frac{\vec{S}_{Rx,con} + \vec{S}_{Tx,con}}{2}. \quad (19)$$

The presented algorithm cannot resolve two parallel lines. This can only occur in the case of a path with more than one reflection. Since these rays are not accessible anyway, this issue is not important.

The algorithm is transferable to extended objects with scattering. After a deconvolution algorithm without noise enhancement, the received amplitudes for each beam steering

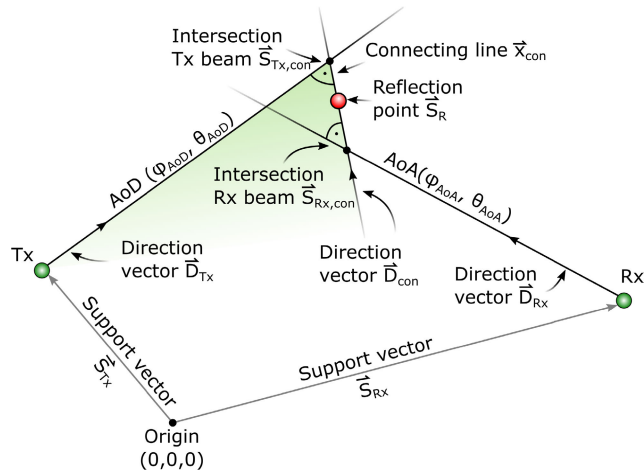


FIGURE 10. Sketch of the Tx, Rx, and the scattering center including all vectors employed to compute the reflection points. The green shaded area is created by the directional vectors \vec{D}_{Tx} and \vec{D}_{Con} and indicates a part of \vec{x}_{plane} .

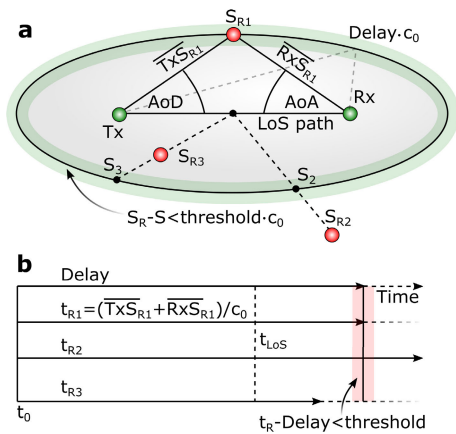


FIGURE 11. Classification of the reflection points. **a:** In spatial domain, the delay of the peaks determines an ellipsoidal solution space, where reconstructed reflection points of rays with one reflection can be found. Peaks with a distance to the ellipsoid that exceeds the threshold are classified as “class 3: > 1 reflection”. The green area shows the accepted distance below the threshold. **b:** In temporal domain, the delay t_R of the assumed propagation paths is compared to the detected delay. For small differences in delay below the threshold (red shaded area), reflection points are still classified as “class 2: 1 reflection”. Note that the threshold condition is different for the spatial and the temporal domain as indicated by the different colors.

angle, i.e., the AoD and AoA are connected to a receive amplitude. From this, the reflection points can be computed exactly in the same way as described above. Extended objects would appear then as a cloud of points with an amplitude in 3D space. The amplitudes could be corrected by the free-space path loss, thus providing information about the reflection characteristics of the objects. Connecting the dots to an extended object via interpolation requires a rescaling of the amplitudes since they are mapped from equidistant angles to an elliptical coordinate system.

c: CLASSIFICATION OF THE RAYS

In this step, the individual components of the CIR are classified in LoS, one reflection, and more than one reflection. In addition, since this clear classification is not

always possible, two more classes were implemented: A class for invalid reflection points containing, e.g., “NaN”s and a class for reflection points that are not classifiable. For the classification of reflection peaks, we use the delay as additional information as depicted in Fig. 11. Since in measurements, the absolute path delay is unknown, we also do not take it for granted in our simulation that should be finally able to handle measurements as an input after the verification employing the raytracing simulation.

For a calibration of the time axis, the LoS component of the CIR can be used. So for each combination of Tx and Rx, the global angles of the first peak are checked, if they are similar (deviation < 10°). If they are, we assume that this peak is a LoS component, i.e., “class 1”. Since the distance between Tx and Rx is known, the time axis can be calibrated.

Using this calibrated time axis, we compare the delays detected in the first step of the algorithm with the delays obtained from the path from the Tx to the reflection point to the Rx (s. Fig.: 11b). If the difference between these two delays is below a certain threshold, in our case 936 ps (≈ 28 cm), given by the pulse duration and 3dB bandwidth, then we assume that the peak can be associated to a ray of the first reflection order (“class 2”). If the time difference between the two delays exceeds the threshold, we assume that the ray had more than one reflection on its path (“class 3”).

Reflection points with “NaN”s in their coordinates cannot be associated to reflection orders (“class 4”), although the issues most likely results from parallel beams with two reflections, which have the same distance from each other in all points of the line and thus don’t have an unambiguous solution for the equation systems presented above in Par. III-B0b.

In case the first peak is not an LoS component, we implemented a kind of majority decision, starting with the given, presumably arbitrary time axis. If the CIR contains two peaks of the first reflection order, those two have the same time difference (deviation < threshold) between the detected delay and the delay resulting from the path length and this information can be utilized for time calibration. For only one peak of first reflection order, the time axis cannot be calibrated and all peaks within the CIR cannot be classified (“class 5”).

In an intermediate state of the code, we evaluated the spatial distance between the reflection point and the ellipsoid of solutions given by the detected delay (s. Fig.: 11a). This condition is a little bit different from comparing the delays. Although we employed the same threshold condition translated into a distance, the recognition of first order reflections was less reliable.

C. COMPUTATIONAL COMPLEXITY ANALYSIS

As already mentioned, our algorithm for estimating the position of reflectors based on CIR measurements has a lower computational effort than state-of-the-art methods like the MUSIC algorithm. This can be proven by an analysis of the computational complexity resp. effort.

In [32], the computational complexity costs for ESPRIT, 2D-MUSIC and RD-MUSIC algorithms are found to be

$$O(LM^2P^2 + M^3P^3 + K^3), \quad (20)$$

$$O(LM^2P^2 + M^3P^3 + n^2M^2P^2) \quad (21)$$

respectively

$$O(LM^2N^2 + M^3N^3 + n[(M^2N + M^2)(MN - K) + M^2]). \quad (22)$$

M denotes the number of elements of the transmit phased array, N the number of elements of the receive phased array, K the number of targets (i.e. reflectors), L the number of signal samples, P the interpolation factor and n the number of iterations. In general, the iteration number n should be much larger than L, M and P. It can be seen that the costs for ESPRIT and 2D-MUSIC are only derived for one phased array (either TX or RX) and, therefore, just for detection of the AoA (or AoD), whereas the RD-MUSIC analysis includes phased arrays for TX and RX, but does not incorporate an interpolation factor of the signal samples. Nevertheless, the computational effort of those algorithms can be approximated to be of cubic polynomial order with respect to both, the number of antenna elements and the interpolation factor.

It is important to mention that MUSIC and ESPRIT are designed for digital beamforming systems. Nevertheless, these algorithms can also be used for analog beamforming systems. In such a case, orthogonal beams are used to generate the input matrix (beam-space MUSIC resp. beam-space ESPRIT). The number of orthogonal beams is equivalent to the number of elements in the phased array. Thus, M and N in the complexity costs given above correspond to the number of TX resp. RX beams.

In our 'compare pattern' algorithm, the AoD, AoA and ToF are jointly estimated. To be able to compare the results of the computational complexity analysis with the previously shown results of the state-of-the-art algorithms, we define M_b as the number of TX beams, N_b as the number of RX beams, and L_s as the number of CIR samples. We furthermore define M_c , N_c resp. L_c as the number of beams resp. CIR samples in a local surrounding of the identified peak (i.e. the cutout region). Finally, we define P_b as the oversampling factor of the antenna pattern and P_t as the interpolation factor of the CIR pulses. Please note, that for this analysis, we just use the total number of beams instead of separating them into the elevation and azimuth angles. The results are the same, but the equations are easier to read.

The proposed algorithm consists of four major steps:

- 1) Finding the maximum peak in a $M_b \times N_b \times L_s$ matrix and extract a cutout region of interest of size $M_c \times N_c \times L_c$
- 2) Generate a multi-dimensional comparison matrix of the super-resolution angular antenna patterns and all possible high-resolution pulses in the cutout region of size $M_c \times N_c \times L_c \times M_c P_b \times N_c P_b \times L_c P_t$

- 3) Correlate the cutout region of the received signal with the comparison structure.
- 4) Identify the correlation peak and extract AoD, AoA and ToF

The computational effort for the first two steps is linear with the size of the appropriate matrix. In the worst case, we need to access each element once. For the third step, we need to iterate the cutout region over the whole multi-dimensional comparison matrix and perform an element-wise multiplication of $M_c \times N_c \times L_c$ elements. Such element-wise operation is of linear effort with respect to the number of elements, $O(M_c N_c L_c)$. The element-wise multiplication is repeated in $P_b M_c \times P_b N_c \times P_t L_c$ iterations with a shifted cutout region. Thus, the complexity for the third step is given by $O(M_c^3 N_c^3 P_b^2 L_c^2 P_t)$. The final identification of the correlation peak is again a linear search over $M_c P_b \times N_c P_b \times L_c P_t$ elements with effort $O(M_c N_c P_b^2 L_c P_t)$. Thus, the total computational complexity costs of our algorithm is given by

$$O(M_b N_b L_s + M_c^2 N_c^2 P_b^2 L_c^2 P_t + M_c^3 N_c^3 P_b^2 L_c^2 P_t + M_c N_c P_b^2 L_c P_t). \quad (23)$$

On first sight, the effort of the proposed algorithm is also of cubic polynomial order. But it is of cubic polynomial order with respect to the number of beams in the cutout region. This number is usually a fixed parameter and not changed when increasing the number of beams resp. the number of phased array elements. For our simulation presented in Section IV, we used the two adjacent beams to define the cutout region, i.e. $M_c = N_c = 3$. To compare with the state-of-the-art algorithms, the dependencies on the number of beams, signal samples resp. the interpolation factor have to be considered. They are of linear resp. quadratic order. Taking just the relevant dependencies into account and removing the constants, equation (23) can be shortened to

$$O(M_b N_b L_s + P_b^2 L_c^2 P_t + P_b^2 L_c P_t). \quad (24)$$

Thus, it is shown that the proposed algorithm has lower computational complexity compared to state-of-the-art algorithms like MUSIC and ESPRIT.

IV. SIMULATION RESULTS

In this section, the simulation results for a reconstruction of the reflection points are presented. We start with an evaluation of the angle detection, coming to the computation of the 3D reflection points and continue with the classification algorithm.

A. DETECTION ACCURACY OF THE ANGULAR AND TEMPORAL INFORMATION

From the structure A_{CIR} , (cf. (3)), the azimuth and elevation components of the AoD and AoA are extracted for each peak above the detection threshold, together with the path delay. To evaluate the results of the angular analysis systematically,

we skip the specific room geometry and use the data set B_{CIR} (cf. (7)) without the temporal component.

We decided for a step size of 5° between different ray angles, since it offers a good compromise between computation time and meaningful results: An optimal performance of the 'find maximum' algorithm would result in an average deviation of 2.5° , which is same as for an infinitely small step size. The maxima of the azimuth and elevation angle, $\pm 60^\circ$ and $\pm 20^\circ$ are as large as the range of beam steering angles in order to evaluate the limits of the algorithm for different array sizes.

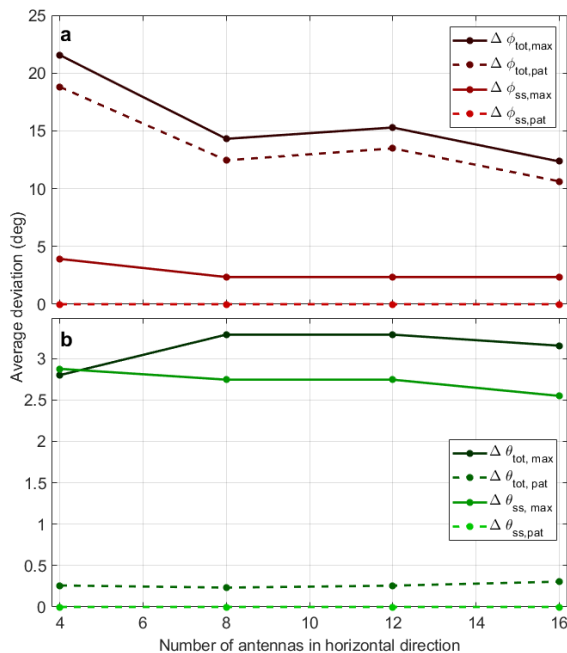


FIGURE 12. Average deviation between detected and simulated AoD. Comparison between the two methods, which are the detection of the maximum ("max") and the comparison of the antenna patterns. For a subset of angles ($|\text{az}| < 40^\circ$, "ss"), the deviation is substantially smaller. **a:** Azimuth angle ϕ . **b:** Elevation angle θ .

Figure 12 shows the difference between the detected angle and the simulated ("true") AoD. We compared four different types of evaluation: the simple 'find maximum' algorithm (index "max") and the more complex algorithm of comparing different antenna patterns in a region of interest (index "pat"), both for either the complete range of angles or for a specific subset of angles ($|\phi| < 40^\circ$, $|\theta| < 20^\circ$). The more complex method of comparing the antenna patterns is about 2.5° better than the 'find maximum' algorithm. For larger antenna arrays, i.e. smaller beam width, the difference between the detected and the simulated beam decreases, approaching for the subset and the maximum method the theoretical limit of 2.5° .

For the elevation angle, depicted in Fig. 12b, the average deviation between the detected and the simulated angle is way smaller with maximally around 3° . Here, the largest difference can be found between both methods of analysis, with the comparison of patterns showing the better results. The performance of the algorithm does not depend significantly

on the number of antennas in horizontal direction, since this does not change much of the beam width in vertical/elevation direction.

The structure of the data set is fully symmetric. Thus, the results for the AoA are the same as for the AoD and do not need to be shown in a separate figure. In general, we can conclude from Fig 12, that the 'compare patterns' method works always better than the 'find maximum' algorithm and that the results are better for the subset of rays. In addition, larger antenna arrays with a small beam width facilitate a more accurate detection of angles.

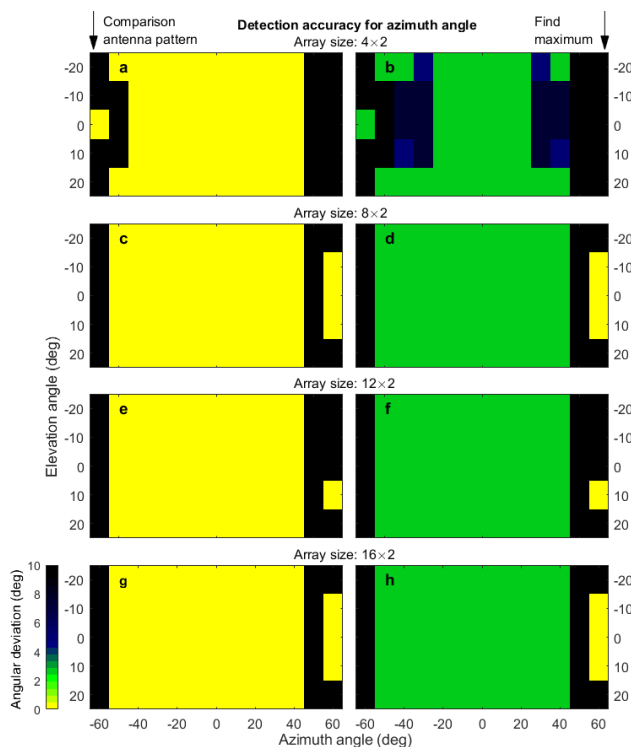


FIGURE 13. Detection error of the azimuth angle as a function of the local angle. Comparison of two different detection methods for four different array sizes. Left column: Comparison of the antenna patterns, right column: Find maximum. The array size is varied in horizontal direction from 4 in the upper line to 16 antennas in the lower line.

The error of the angle extraction from B_{CIR} is depicted in Figs. 13 and 14 as a function of the local angle for the azimuth and the elevation direction, respectively. The left column in both figures shows the results for the comparison of antenna patterns, and the right side the results for the maximum detection algorithm. Each ray is counted twice in this diagram, once for the Tx azimuth and elevation angle and once for the Rx angles.

The azimuth error (Fig. 13) is increasing for large local azimuth angles $|\phi| > 40^\circ$, where the sidelobes are growing. For azimuth angles $|\phi| < 40^\circ$, the angular deviation is close to zero for the comparison of patterns and about 2.5° for the 'find maximum' algorithm. The results do not depend strongly on the elevation angle.

The error of the elevation angle, shown in Fig. 14, shows a different behavior. The error in elevation does not depend

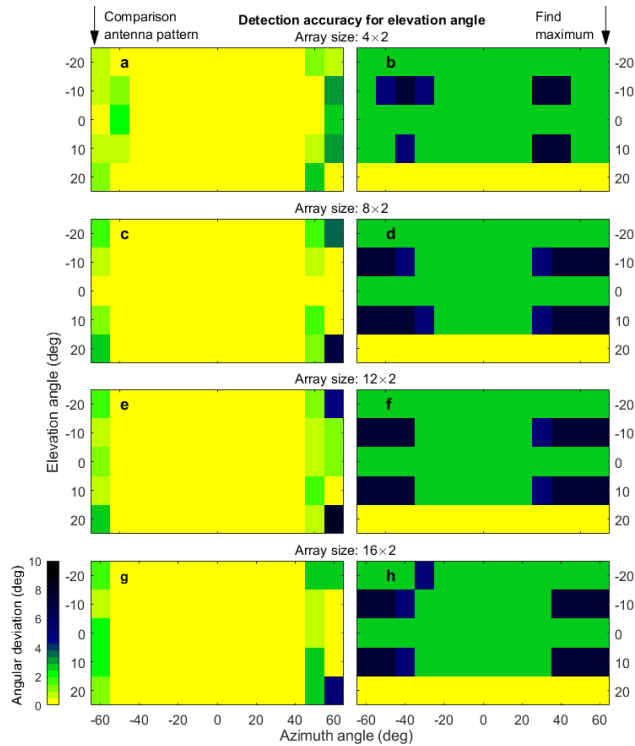


FIGURE 14. Detection error of the elevation angle as a function of the local angle. Comparison of two different detection methods for four different array sizes. Left column: Comparison of the antenna patterns, right column: Find maximum. The array size is varied in horizontal direction from 4 in the upper line to 16 antennas in the lower line.

significantly on the array size, since the beam width in elevation direction does not change much. However, the accuracy of the elevation angle extraction relies on the local azimuth angle: For azimuth angles $> |40^\circ|$, the detection accuracy decreases a little. This indicates that the detection of azimuth and elevation angles is not completely independent from each other. The slight asymmetry of the figures in azimuth and elevation direction is due to the rounding of the rays in 5° steps.

The detection of the delay of the individual peaks as a function of the number of antennas in horizontal direction is plotted in Fig. 15. 73 peaks were detected in total, for all combinations of Tx and Rx. The dashed line shows the result that we would expect for randomly distributed path delays. For the maximum search algorithm this would be a quarter of the sampling period (41.7 ps) and for the pattern comparison method one tenth of it since $m_{t,peak}$ was set to 10. All the results are a little above that theoretical value, indicating some small detection errors. The results do not rely on the number of antennas in horizontal direction, since the number of antennas does not affect the shape of the pulse in the temporal direction.

B. RECONSTRUCTION OF 3D REFLECTION POINTS

The raytracing model for the scenario from Fig. 2 consists of 73 rays in total. Some are out of the beam steering range, and some contain multiple reflections which cannot be handled

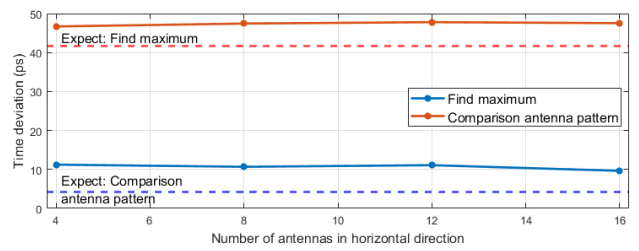


FIGURE 15. Accuracy of the peak time detection for the 'Find maximum' and the 'Compare patterns' method. The dashed line indicates the expectation for equally distributed peak times.

as shown in Section III-Bb. We, furthermore, limit the room reconstruction to azimuth angles $|\phi| < 40^\circ$, where the best performance of the angular detection is given. Thus, a subset of 6 rays is used for the evaluation, as shown in Fig. 17.

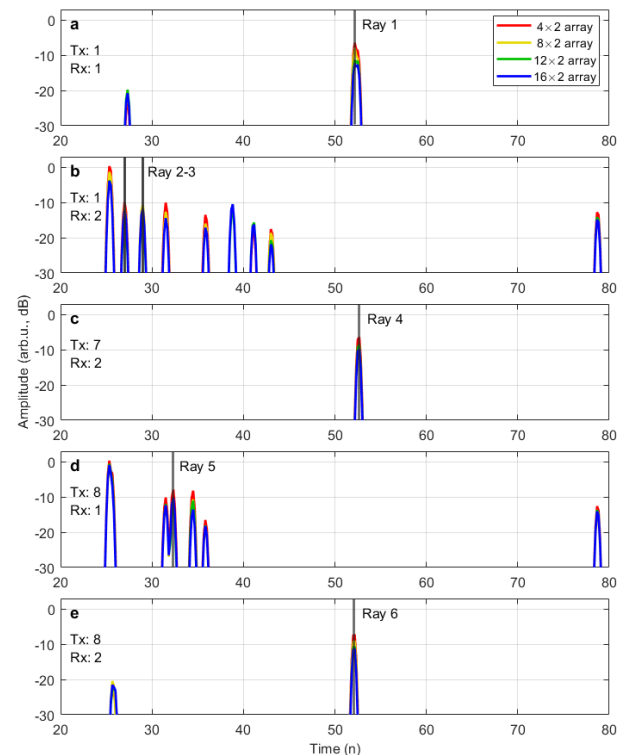


FIGURE 16. CIRs for the reconstructed rays as a function of time, averaged over all beam steering angles for all array sizes. a: For Tx_1 and Rx_1 . b: For Tx_1 and Rx_2 . c: For Tx_7 and Rx_2 . d: For Tx_8 and Rx_1 . e: For Tx_8 and Rx_2 .

The reconstruction of the reflection points, including the AoA, AoD, and the path delay as well as the deviation between the reconstructed reflection points and the simulated ones are listed in Tab 2 for different array sizes between 4 and 16 antennas in horizontal direction. The angle-averaged CIRs in which the respective multipath components appear are depicted in Fig. 16 for all array sizes.

The first reflection point is reconstructed with the relatively high accuracy of 7 cm for array sizes of 8 and 12 antennas. For 16 antennas, the reconstruction is not performing well due to deviations in the detection of angles. Figure 16a shows two partially overlapping peaks at 52-53 ns, which could make it difficult at least for some array sizes to identify the

TABLE 2. Reconstruction of the reflection points. “sim” stands for the simulated, “true” information of the ray. “rec” stands for the reconstructed reflection points and beam parameter values. $n \times m$ gives the array size. The coordinate system of the Reflection points is designed in a way that the x- and y-axis are in horizontal plane and the z axis points in vertical direction.

Ray	sim/rec ($n \times m$)	AoD_{local} (az (deg), el (deg))	AoA_{local} (az (deg), el (deg))	Delay (ns)	Reflection (x(m); y(m); z(m))	$ \vec{S}_{rec} - \vec{S}_{sim} $ (m)
1	sim	-4.0; 0.0	4.0; 0.0	52.2	5.95; 8.00; 1.00	-
	rec (4 × 2)	-4; 0	3; 0	52.2	6.029; 9.19; 1.00	1.194
	rec (8 × 2)	-4; 0	4; 0	52.2	5.95; 8.07; 1.00	0.065
	rec (12 × 2)	-4; 0	4; 0	52.2	5.95; 8.07; 1.00	0.065
	rec (16 × 2)	-4; -10	4; 10	51.8	6.0; 1.2644; 1.00	6.736
2	sim	28.9; 0	-28.9; 0	29.0	3.50; 3.64; 1.00	-
	rec (4 × 2)	29; 0	-29; 0	29.0	3.49; 3.64; 1.00	0.006
	rec (8 × 2)	29; 0	-29; 0	29.0	3.49; 3.64; 1.00	0.006
	rec (12 × 2)	29; 0	-29; 0	29.0	3.49; 3.64; 1.00	0.006
	rec (16 × 2)	29; 0	-29; 0	29.0	3.49; 3.64; 1.00	0.006
3	sim	-20.2; 0.0	20.2; 0.0	27.0	7.00; 4.54; 1.00	-
	rec (4 × 2)	-20; 0	20; 0	27.0	6.98; 4.55; 1.00	0.018
	rec (8 × 2)	-20; 0	20; 0	27.0	6.98; 4.55; 1.00	0.018
	rec (12 × 2)	-20; 0	20; 0	27.0	6.98; 4.55; 1.00	0.018
	rec (16 × 2)	-20; 0	20; 0	27.0	6.98; 4.55; 1.00	0.018
4	sim	8.4; 0.0	-8.4; 0	52.6	4.65; 0.00; 1.00	-
	rec (4 × 2)	8; 0	-8; 0	52.6	4.65; -0.38; 1.00	0.383
	rec (8 × 2)	8; 0	-8; 0	52.6	4.65; -0.38; 1.00	0.383
	rec (12 × 2)	8; 0	-8; 0	52.6	4.65; -0.38; 1.00	0.383
	rec (16 × 2)	8; 0	-8; 0	52.6	4.65; -0.38; 1.00	0.383
5	sim	-38.3; 0.0	38.3; 0.0	32.3	3.50 4.00; 1.00	-
	rec (4 × 2)	-38; 0	38; 0	32.3	3.53; 4.00; 1.00	0.031
	rec (8 × 2)	-38; 0	38; 0	32.3	3.53; 4.00; 1.00	0.031
	rec (12 × 2)	-38; 0	38; 0	32.3	3.53; 4.00; 1.00	0.031
	rec (16 × 2)	-38; 0	38; 0	32.3	3.53; 4.00; 1.00	0.031
6	sim	-2.6; 0.0	2.6; 0.0	52.1	6.15; 0.00; 1.00	-
	rec (4 × 2)	-2; 0	2; 0	52.1	6.15; -2.22; 1.00	2.222
	rec (8 × 2)	-2; 0	3; 0	52.1	6.22; -0.22; 1.00	0.227
	rec (12 × 2)	-1; 0	1; 0	52.1	6.15; -12.25; 1.00	12.252
	rec (16 × 2)	-2; 0	2; 0	52.1	6.15; -2.22; 1.00	2.222

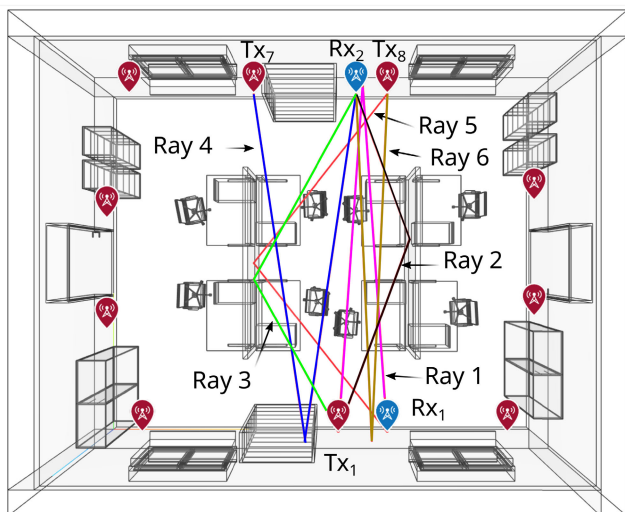


FIGURE 17. Simulated rays 1-6 in the office room scenario.

angles correctly and thus, to compute the correct reflection point. In our angle detection algorithm, we have an angular resolution of one degree. Although the angles were perfectly detected with the given resolution for 8 and 12 antennas, 7 cm of deviation remain. The reconstructed ray has a small angle at the reflection point (s. Fig.: 17) which means that even sub-degree angular deviations significantly influence

the position of the reflection point. This can be also seen for ray 4 (s. Fig.: 16c) and for ray 6 (s. Fig.: 16e), with an especially large effect.

Considering now the average angular deviation of 2.5° degree for the detection of maxima with 10° steps, the advantage of the method of comparing the antenna patterns becomes clear. For the rays 2, 3, and 5 (s. Fig.: 16b,d), the angle at the reflection point is large and the reflection point is computed with 0.6, 1.8, and 3.1 cm difference to the reflection point in the raytracing model.

C. CLASSIFICATION ALGORITHM

The correct classification of rays depends on the features of the complete CIR for the respective Tx-Rx pair. From the six rays with one reflection in the angular range of $|\phi| < 40^\circ$ and $|\theta| < 20^\circ$, only three are correctly identified as first reflection order. Those are ray 2, 3, and 5. Rays 1, 4, and 6 cannot be identified as first reflection order without additional information for the calibration of the time axis, since they are the only rays in their CIR with only one reflection.

V. DISCUSSION

In the presented room reconstruction procedure, the extraction of the AoD, AoA, and delay from the received CIRs of a full beam scan are the most complex operations. The

following steps of determining the 3D scattering points based on the extracted information and the classification of the reflections are relatively straight forward. The simulation results show, how sensitive the position of the scattering points depends on the correct detection of the angles. Therefore, the first step of the signal processing, the extraction of the relevant parameter values, is of utmost importance and has to provide a high angular resolution.

The simulation results presented in the previous Section IV show that the performance of the room reconstruction is strongly improved by using the 'compare pattern' approach. The angle detection is improved by 2.5° compared the 'find maximum' method, independent of the number of antenna patches and, therefore, the beam width. For azimuth angles $|\phi| < 40^\circ$, the angular deviation of 'compare pattern' is close to zero.

While the results in Fig. 12a show the expected behaviour that an increasing number of antenna patch elements - and, therefore, a decreased beam width - decreases the average angular deviation, another effect can also be notified: For a subset of beams with azimuth angle of $|\phi| < 40^\circ$, the average deviation is much smaller. This indicates that the overall angular deviation is mainly determined by large azimuth angles, and not the beam width itself. This conclusion is supported by the results from Fig. 12b. In elevation direction, the beam is less focused than in azimuth direction, since only two rows of antenna elements are used in vertical direction. While worse results than for the azimuth angle would be expected, the performance is comparable. The reason is that the elevation angle evaluation was limited to $\pm 20^\circ$.

The explanation for the described effect are the side lobes of the antenna pattern, which are increasing for large beam steering angles, i.e. azimuth angles $|\phi| > 40^\circ$. For these angles, the maximum peak in the structure A_{CIR} is identified in a side lobe far away from the real beam by the 'find maximum' method, as shown in Fig. 13. Since the 'compare patterns' method is only applied to a region of interest in a $\pm 10^\circ$ surrounding of a peak identified by 'find maximum', its performance is drastically reduced. In contrast, the detection error for the elevation angle shows a different behaviour (Fig. 14). Since the beam scanning range is limited to $|\theta| < 20^\circ$, the peak identified by 'find maximum' will always be within the main lobe. Therefore, 'compare patterns' can correct the detection error and improve the results.

The rays in Fig. 17 show that only a small area between the two screens is scanned in our scenario. The screens block horizontal beams effectively, and apparently, there were no reflections at the ceiling that matched the criterion of angles ($|\phi| < 40^\circ$ and $|\theta| < 20^\circ$). A different room geometry and a different distribution of Tx and Rx within the room would increase the number of beams that could be utilized for room reconstruction.

In summary, the proposed 'compares pattern' method always improves the results from 'find maximum'. Since its current implementation relies on the peak identified by 'find maximum', its improvements are especially shown in

scenarios with a limited beam scanning range. Even wide beams (small patch array antennas) can be used, leading to fast scanning times. Using another method for the first step of peak identification would improve the performance for large scanning angles. This could be either an extension of the pattern matching to the whole structure (and not only a region of interest) or the use of a different method like a maximum likelihood method.

When using the current implementation of the proposed room reconstruction method, the following conditions need to be fulfilled for a successful reconstruction:

- The ray has to be of first reflection order.
- The ray has to be within the field of view (here $\phi < |60^\circ|$, $\theta < |20^\circ|$) for both, AoD and AoA.
- The ray must be within the angular range, were the beam pattern allows for unambiguous angle detection (here $\phi < |60^\circ|$) for both, AoD and AoA.
- In addition, the correct classification (i.e. first order reflection) of the ray must be possible. I.e., either the CIR contains a LoS component or at least two rays of first reflection order that fulfill the preceding requirements.
- In addition, the results are more reliable, if the peak of the ray is not overlapping with another multipath component.

The proposed room reconstruction method only uses the angular information for the reconstruction of reflection points. The path delay is used for the classification of the peaks. The reflection points could be reconstructed with potentially higher accuracy by also computing the intersections of the Tx and Rx lines with the ellipsoid given by the path delays and computing the mean of these three possible reflection points.

A. IMPACT OF ADDITIONAL PHYSICAL EFFECTS

The used raytracing simulation model to construct the CIRs is essentially a representation of geometrical optics applied for radio waves. Thus, it is a good approximation for large distances and objects that are by far larger than the wavelength. We do not consider effects based on the wave characteristics of electromagnetic radiation such as scattering, diffraction, (semi-) transmission through objects, or the polarization of waves. The impact of these effects depends highly on the geometry of the room, the material of the objects inside the room, and the wavelength of the radiation.

Scattering would lead to the visibility of extended objects as a convolution of the object with $A_{Pat, TxRx, t}$ (cf. (6)), i.e., the multipath components in the CIR would be broader peaks in time and angle. Thus, a different deconvolution algorithm has to be employed. Besides this, the subsequent steps in the room reconstruction algorithm can remain the same.

Diffraction requires a completely different approach for room reconstruction, depending on the wavelength and the distance of the object causing the diffraction. Typical objects that lead to diffraction are sharp edges or a small slit with a

TABLE 3. Physical effects, impact on CIRs and room reconstruction algorithms, countermeasures and potential benefits.

Effect	Impact on CIR	Impact on room reconstruction	Suggested algorithmic treatment	Possible benefits for room reconstruction
Scattering	Relatively strong impact with broader peaks in time and angle	Objects appear as point clouds	Modify first step of the algorithm by using maximum likelihood algorithm or extended pattern matching algorithm	Reconstruction of spatially extended objects from a single point of view; contributes to surface characterization
Diffraction	Appears as “point target” at the diffracting structure; depending on the room geometry mostly small impact in CIR	Overly pronounced edges	-	Clear outline of objects
Refraction (“transmission through objects”)	Attenuated component of CIR, therefore small impact	Possible shift of objects	-	-
Polarization	Separate CIRs for both linearly independent directions of polarization	Same algorithm applied to both directions of polarization	Separate reconstruction for both directions of polarization	Contributes to material characterization
Hardware impairments	Stretching, rotation and offset of the CIRs in the IQ diagram	Negative impact on accuracy	Correction for hardware impairments provided by communication hardware	-
Noise	In a first approximation equally distributed among all angles and arrival times.	Negative impact on accuracy	Prohibits application of zero forcing and matrix inversion algorithms	-

size in the order of the wavelength. As long as there are no objects in the room that resemble diffraction grids or other kind of meta-surfaces, the diffraction component in a channel impulse response can be considered to be small compared to other components of the channel impulse response. Signal components that stem from single sources of diffraction would appear similar to point targets, i.e., the end of a wall would appear especially pronounced in a reconstructed image of a room.

Taking into account *polarization* does not provide principally different results, it just adds an additional degree of complexity to the CIR and could be potentially used for material characterization.

The additional effects expected for real measurements, their impact on room reconstruction and suggested countermeasures as well as possible benefits are summarized in Tab. 3.

VI. CONCLUSION AND OUTLOOK

We evaluated the performance of a three-step method for room reconstruction employing simulated channel impulse responses in an exemplary office room. The method consists of the extraction of AoD and AoA, the computation of possible reflection points and the classification of rays within the CIR into direct path, first order reflection path and paths with more than one reflection. We compared two algorithms for the extraction of AoD and AoA in a raytracing simulation environment. The evaluation shows that the ‘*compare pattern*’ algorithm outperforms the simple ‘*find maximum*’ approach.

The presented theoretical study serves as a foundation for our future experimental work. Our results provide an estimation of the performance of a room reconstruction algorithm that can be expected from a certain accuracy in angle

estimation. It also indicates some of the potential pitfalls of room reconstruction, e.g., using triangles to detect targets with a small angle relative to the transceivers, ambiguities in antenna patterns, or a non-optimal distribution of transceivers within the room. Optimizing the transceiver position in the room for communication is not the same as optimizing for room reconstruction, since RADAR requires reflections and communication works well with the minimization of reflections. Note that side lobes in antenna patterns can be handled relatively easily if the antenna patterns are accurately known.

These constraints should be considered in the planning of a JCAS system. Our simulations facilitate finding the optimal settings for the respective experimental systems. Future topics in the context of room reconstruction could be the reconstruction of extended, scattering objects instead of point targets and the inclusion of dynamics including the Doppler effects. The minimization of the overall reconstruction error in a multi-static sensing system could, e.g., utilize historic information about the local environment. For real-time implementations, an optimal combination of methods, including analytical and numerical approaches as well as tools from artificial intelligence, must be found in a trade-off between performance and simplicity of realization. In the future, we aim for an implementation of our sensing methods in a real-time JCAS system.

REFERENCES

- [1] D. K. P. Tan, J. He, Y. Li, A. Bayesteh, Y. Chen, P. Zhu, and W. Tong, “Integrated sensing and communication in 6G: Motivations, use cases, requirements, challenges and future directions,” in *Proc. 1st IEEE Int. Online Symp. Joint Commun. Sens. (JCS)*, Dresden, Germany, Feb. 2021, pp. 1–6.
- [2] T. Wild, V. Braun, and H. Viswanathan, “Joint design of communication and sensing for beyond 5G and 6G systems,” *IEEE Access*, vol. 9, pp. 30845–30857, 2021.

- [3] M. A. Uusitalo, P. Rugeland, M. R. Boldi, E. C. Strinati, P. Demestichas, M. Ericson, G. P. Fettweis, M. C. Filippou, A. Gati, M.-H. Hamon, M. Hoffmann, M. Latva-Aho, A. Pärssinen, B. Richerzhagen, H. Schotten, T. Svensson, G. Wikström, H. Wymersch, V. Ziegler, and Y. Zou, "6G vision, value, use cases and technologies from European 6G flagship project Hexa-X," *IEEE Access*, vol. 9, pp. 160004–160020, 2021.
- [4] J. A. Zhang, M. L. Rahman, K. Wu, X. Huang, Y. J. Guo, S. Chen, and J. Yuan, "Enabling joint communication and radar sensing in mobile networks—A survey," *IEEE Commun. Surveys Tuts.*, vol. 24, no. 1, pp. 306–345, 1st Quart., 2022.
- [5] H. Viswanathan and P. E. Mogensen, "Communications in the 6G era," *IEEE Access*, vol. 8, pp. 57063–57074, 2020.
- [6] N. Zeulin, A. Ponomarenko-Timofeev, O. Galinina, and S. Andreev, "ML-assisted beam selection via digital twins for time-sensitive industrial IoT," *IEEE Internet Things Mag.*, vol. 5, no. 1, pp. 36–40, Mar. 2022.
- [7] S. Y. Lee, Z. Majid, and H. Setan, "3D data acquisition for indoor assets using terrestrial laser scanning," *ISPRS Ann. Photogramm., Remote Sens. Spatial Inf. Sci.*, vol. 2, pp. 221–226, Sep. 2013.
- [8] R. Schmidt, "Multiple emitter location and signal parameter estimation," *IEEE Trans. Antennas Propag.*, vol. AP-34, no. 3, pp. 276–280, Mar. 1986.
- [9] R. Roy and T. Kailath, "ESPRIT-estimation of signal parameters via rotational invariance techniques," *IEEE Trans. Acoust., Speech, Signal Process.*, vol. 37, no. 7, pp. 984–995, Jul. 1989.
- [10] Y. Sun, J. Li, T. Zhang, R. Wang, X. Peng, X. Han, and H. Tan, "An indoor environment sensing and localization system via mmWave phased array," *J. Commun. Inf. Netw.*, vol. 7, no. 4, pp. 383–393, Dec. 2022.
- [11] R. S. Thoma, O. Hirsch, J. Sachs, and R. Zetik, "UWB sensor networks for position location and imaging of objects and environments," in *Proc. 2nd Eur. Conf. Antennas Propag. (EuCAP)*, 2007, pp. 1–9.
- [12] Y. Miyake, M. Kim, and J.-I. Takada, "Development of room geometry estimation technique utilizing millimeter-wave radio systems," *IEICE Commun. Exp.*, vol. 10, no. 9, pp. 647–651, Sep. 2021.
- [13] E. Sedunova, N. Maletic, L. Wimmer, D. Cvetkovski, E. Grass, and B. Lankl, "Utilizing beamsteering at millimeter waves for indoor object and room geometry detection," in *Proc. IEEE 4th 5G World Forum (5GWF)*, Montreal, QC, Canada, Oct. 2021, pp. 340–345.
- [14] B. Li, X. Wang, E. Au, and Y. Xin, "Joint localization and environment sensing of rigid body with 5G millimeter wave MIMO," *IEEE Open J. Signal Process.*, vol. 4, pp. 117–131, 2023.
- [15] J. Palacios, N. González-Prelcic, and C. Rusu, "Multidimensional orthogonal matching pursuit: Theory and application to high accuracy joint localization and communication at mmWave," 2022, *arXiv:2208.11600*.
- [16] W. Yu and W. B. Kleijn, "Room geometry estimation from room impulse responses using convolutional neural networks," 2019, *arXiv:1904.00869*.
- [17] J.-Y. Lee, Y. Kim, S. Lee, W. Cho, and S.-C. Kim, "Estimation of room shape using radio propagation channel analysis," *IEEE Sensors J.*, vol. 19, no. 24, pp. 12316–12324, Dec. 2019.
- [18] M. Crocco, A. Trucco, and A. D. Bue, "Uncalibrated 3D room reconstruction from sound," 2016, *arXiv:1606.06258*.
- [19] Y. E. Baba, A. Walther, and E. A. P. Habets, "3D room geometry inference based on room impulse response stacks," *IEEE/ACM Trans. Audio, Speech, Lang. Process.*, vol. 26, no. 5, pp. 857–872, May 2018.
- [20] W. B. Abbas, F. Gomez-Cuba, and M. Zorzi, "Millimeter wave receiver efficiency: A comprehensive comparison of beamforming schemes with low resolution ADCs," *IEEE Trans. Wireless Commun.*, vol. 16, no. 12, pp. 8131–8146, Dec. 2017.
- [21] M. Goodarzi, V. Sark, N. Maletic, J. G. Terán, G. Caire, and E. Grass, "DNN-assisted particle-based Bayesian joint synchronization and localization," *IEEE Trans. Commun.*, vol. 70, no. 7, pp. 4837–4851, Jul. 2022.
- [22] Software. *Revit LT & Revit LT Suite*. Accessed: Jun. 27, 2024. [Online]. Available: <https://www.autodesk.de/products/revit-lt/overview>
- [23] L. B. Lucy, "An iterative technique for the rectification of observed distributions," *Astronomical J.*, vol. 79, p. 745, Jun. 1974.
- [24] W. H. Richardson, "Bayesian-based iterative method of image restoration," *J. Opt. Soc. Amer.*, vol. 62, no. 1, pp. 55–59, Jan. 1972.
- [25] A. Viterbi, "Error bounds for convolutional codes and an asymptotically optimum decoding algorithm," *IEEE Trans. Inf. Theory*, vol. IT-13, no. 2, pp. 260–269, Apr. 1967.
- [26] E. Sedunova, N. Maletic, D. Cvetkovski, and E. Grass, "Enhanced object localization using a beamsteering mmWave communication system," in *Proc. 6th Int. Conf. Adv. Commun. Technol. Netw. (CommNet)*, Rabat, Morocco, Dec. 2023, pp. 1–6.
- [27] A. Caciularu and D. Burshtein, "Blind channel equalization using variational autoencoders," in *Proc. IEEE Int. Conf. Commun. Workshops (ICC Workshops)*, May 2018, pp. 1–6.
- [28] J.-M. Attenu and A. Ross, "Time domain nearfield acoustical holography with three-dimensional linear deconvolution," *J. Acoust. Soc. Amer.*, vol. 143, no. 3, pp. 1672–1683, Mar. 2018.
- [29] N. Chu, H. Zhao, L. Yu, Q. Huang, and Y. Ning, "Fast and high-resolution acoustic beamforming: A convolution accelerated deconvolution implementation," *IEEE Trans. Instrum. Meas.*, vol. 70, pp. 1–15, 2021.
- [30] C. Yi and T. Shimamura, "An improved maximum-likelihood estimation algorithm for blind image deconvolution based on noise variance estimation," *J. Signal Process.*, vol. 16, no. 6, pp. 629–635, 2012.
- [31] K. Ehrenfried and L. Koop, "Comparison of iterative deconvolution algorithms for the mapping of acoustic sources," *AIAA J.*, vol. 45, no. 7, pp. 1584–1595, Jul. 2007.
- [32] D. Oh, Y. Li, J. Khodjaev, J. Chong, and J. Lee, "Joint estimation of direction of departure and direction of arrival for multiple-input multiple-output radar based on improved joint ESPRIT method," *IET Radar, Sonar Navigat.*, vol. 9, no. 3, pp. 308–317, Mar. 2015.



LARA WIMMER received the master's and Ph.D. degrees in physics from the University of Göttingen, in 2013 and 2018, respectively.

Since 2018, she has been a Postdoctoral Researcher with the Department of System Architectures, Leibniz-Institut für innovative Mikroelektronik (IHP). Her current research interests include the upcoming 6G standard and the physical layer: joint communication and sensing, physical layer security, and resilience.



MARKUS PETRI received the Dipl.-Ing. degree from TU Berlin, Germany, in 2006, and the Dr.-Ing. degree from BTU Cottbus, Germany, in 2012.

Up to 2009, he worked in the field of vision sensors for industrial automation. From 2009 to 2020, he was a Scientist at Leibniz-Institut für innovative Mikroelektronik (IHP), Frankfurt (Oder), Germany. From 2020 to 2023, he was the Head of Technology Transfer at IHP Solutions GmbH, Germany. Since 2023, he is again with IHP as a Postdoctoral Researcher. His research interests include joint communication and sensing and appropriate PHY-layer hardware architectures.

Dr. Petri is an awardee of the Erwin-Stephan-Price from the Technical University of Berlin.



ECKHARD GRASS received the Dr.-Ing. degree in electronics from the Humboldt University of Berlin, Germany, in 1993.

He was a Senior Lecturer in microelectronics with the University of Westminster, London, U.K., from 1995 to 1999. He is currently the Team Leader of the Wireless Broadband Communications Group, Leibniz-Institut für innovative Mikroelektronik (IHP), Frankfurt (Oder), Germany, and a Professor with the Humboldt University of Berlin. He was actively involved in the definition of the international mmWave standards IEEE802.15.3c and IEEE802.11ad. Furthermore, he is actively involved in the definition and development of 5G and 6G wireless communication systems and has coordinated several large European and national research projects. His research interests include wireless communication systems, digital signal processing algorithms and architectures, spatial multiplexing techniques (MIMO and OAM), and joint communications and sensing (JCAS).

...